Applied Catalysis B: Environmental 340 (2024) 123162

Contents lists available at ScienceDirect

Applied Catalysis B: Environmental

journal homepage: www.elsevier.com/locate/apcatb

Selective coordination activation regulating the selectivity for photocatalytic hydrogenation of α, β-unsaturated aldehyde over Pd/MIL-100(Fe_aCu_b)

Zhiwen Wang [b], Yueyue Kang [b], Yingzhang Shi [b], Cheng Liu [b], Yunni Liu [a], Jun Lin [a,b,*], Jinhong Bi [b,c,**], Ling Wu [b,***]

[a] Department of Chemistry, Renmin University of China, Beijing 100872, People's Republic of China
[b] State Key Laboratory of Photocatalysis on Energy and Environment, Fuzhou University, Fuzhou, Fujian 350116, People's Republic of China
[c] Department of Environmental Science and Engineering, Fuzhou University, Minhou, Fujian 350108, People's Republic of China

ARTICLE INFO

Keywords:
Coordination activation
Photocatalyst
Hydrogenation
MIL-100(Fe/Cu)
α
β-Unsaturated aldehydes

ABSTRACT

Here, the mixed metal nodes MOFs, Pd/MIL-100(Fe_aCu_b), were constructed as photocatalysts for hydrogenation of α, β-unsaturated aldehyde (UAL) under visible light. 1 wt% Pd/MIL-100($Fe_{0.81}Cu_{0.19}$) can convert a range of UAL to saturated aldehydes (SAL) with a high efficiency (≈ 100 %) and selectivity (≈ 98 %). The results of XPS and in situ DRIFTS reveal that UAL can be selectively activated via a coordination of -C═C- on Cu^{2+} sites, determining the high selectivity of the photocatalytic reaction. The mixed metal nodes and Pd clusters can improve the transformation and separation of photogenerated electrons-holes. EPR result suggests that photogenerated carriers can facilitate the generation of H·on Pd/MIL-100($Fe_{0.81}Cu_{0.19}$), enhancing the catalytic activity. A possible mechanism is proposed for elucidating the catalytic processes at the molecular level. This work provides a valuable strategy for tailoring the selectivity of photocatalytic hydrogenation via selective coordination activation.

1. Introduction

α, β-unsaturated aldehydes (UAL) as an important chemical raw material can be hydrogenated to produce a series of fine chemicals via catalysis, such as unsaturated alcohol (UOL), saturated aldehyde (SAL) and alcohol (SOL), thus attracting much attention [1,2]. However, most of the reported catalytic process need to be assisted by additional temperature and pressure, which would cause some troubles for energy and environment [3,4]. Photocatalysis as a green catalytic approach has attracted much attention, serving as an ideal pathway for hydrogenation reaction [5,6]. Therefore, it is necessary to develop a photocatalytic system for hydrogenation of UAL. Recently, some photocatalysts have been developed for UAL hydrogenation, such as Au/SiC [7], MIL-100 (Fe/Al) [8], Fe_xCo@NC [9], Pd/h-BN [10], $SnNb_2O_6$ [11]. However, because both -C═C- and -C═O can be hydrogenated in a catalytic process, the production of single target product is still a valuable and challenging topic, such as to selectively convert UAL to SAL via individually photocatalytic hydrogenating -C═C- [12–14].

It is reported that the product selectivity of a hydrogenation process may be affected by various factors, such as reaction temperature, time, reactant concentration, solvent and hydrogen source [15,16]. Moreover, our previous works found that to selectively activate the specific group of reactant molecules via coordination on catalyst can effectively improve the target product selectivity [17–19]. Thus, it may be beneficial to convert UAL to SAL via creating a photocatalyst with special active sites to selectively activate -C═C. The coordination activation depends on the chemical interaction between reactant molecules and active sites. The electron density of C═C– is mainly distributed in the double bond, while the electron density of –C═O is concentrated around the O atom [20]. Therefore, there are three possible coordination modes for the UAL molecule absorbed on a catalyst with transition metal active sites in Scheme 1. In route I, -C═C- can be coordinated on a metal

* Corresponding author at: Department of Chemistry, Renmin University of China, Beijing 100872, People's Republic of China.
** Corresponding author at: State Key Laboratory of Photocatalysis on Energy and Environment, Fuzhou University, Fuzhou, Fujian 350116, People's Republic of China.
*** Corresponding author.
E-mail addresses: jlin@ruc.edu.cn (J. Lin), bijinhong@fzu.edu.cn (J. Bi), wuling@fzu.edu.cn (L. Wu).

https://doi.org/10.1016/j.apcatb.2023.123162
Received 24 February 2023; Received in revised form 6 August 2023; Accepted 8 August 2023
Available online 9 August 2023

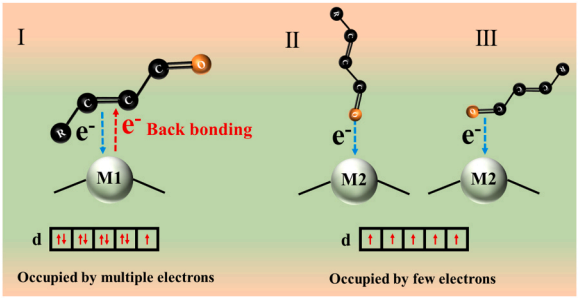

Scheme 1. Possible coordination modes of UAL molecules on the transition metal sites (M) with multiple or few *d* electrons.

atom via transferring π-electron to d orbital. In this case, the d orbitals of metal atom is required to have multiple electrons because the metal with few *d* electrons may prefer to bond -C═O via transferring the lone pair electron of oxygen atom (or the π-electron of C═O) to *d* orbitals (intermediate-II and III). Moreover, abundant d electrons may be transferred to the lowest unoccupied molecular orbital (LUMO) of -C═C- for the formation of back bonding, benefiting to the activation of -C═C-. Therefore, constructing the special metal site with multiple *d* electrons in a catalyst is one of the valid pathways for the selective coordination activation of -C═C-.

Metal-Organic Frameworks (MOFs) as a class of porous materials are widely applied in photocatalysis due to their large specific surface area, versatile metal nodes and tunable organic linkers [21–23], such as MIL-100(Fe) [24], MOF-74(Ni) [25] and Uio-66(Zr) [26]. Particularly, MOFs can provide abundant coordinatively metal sites (CUS) which can be flexibly tuned to adjust interactions between MOFs and reactants, thus regulating the selectivity of products [27,28]. MIL-100(Fe) as a typical MOFs photocatalyst is wildly used to water splitting, CO_2 reduction and organics conversion under visible light [29]. Therefore, MIL-100(Fe) may be an ideal photocatalyst for the hydrogenation reaction. However, MIL-100(Fe) only possess Fe^{3+} sites with five d electrons, thus adverse to coordinating -C═C-. Constructing multi metal nodes MOFs can provide additional active sites. Secondary metal nodes should be introduced which can selectively bond -C═C-. Cu as a IB group element is widely applied as catalyst. Cu^{2+} has highly filled d orbitals with nine d electrons, which may profit to activate -C═C- selectively. But, the Cu-based MOFs have much weak photocatalytic performance under visible light irradiation. Therefore, doping Cu^{2+} ions into MIL-100 (Fe) may be an effective strategy [30]. Moreover, one of the critical pathways for a hydrogenation reaction is the dissociation and activation of hydrogen. The MOFs cannot dissociate H_2. Pd is well-known to have been widely used in hydrogenation reaction because of its outstanding ability for dissociation and activation hydrogen. Pd nanoparticles should be supported on the surface of catalyst as the active sites for the dissociation of H_2. Importantly, the supported Pd can form the Schottky junction with the catalyst to prevent the recombination for photogenerated electron-hole, thus facilitating the generation of active H atoms [31]. Furthermore, deep insight into the interaction between catalyst and reactants may facilitate to recognize the photocatalytic process at a molecular scale.

Here, Pd decorated MIL-100(Fe_xCu_{1-x}) was created as photocatalysts for hydrogenation of UAL to SAL under visible light, such as cinnamyl aldehyde, 3-methyl-2-butenal and acraldehyde. The samples were characterized by SEM, XRD, TEM and UV-DRS. Photo-electrochemistry characterization was used to analyse the transfer and separation ability of the photogenerated electrons-holes. The coordination activation of reactants was detected by in situ EPR and In-situ DRIFTS. Finally, we proposed a possible photocatalytic mechanism for hydrogenation of UAL to SAL on the prepared catalyst.

Table 1
ICP-AES results of Pd/MIL-100(Fe_aCu_b) samples.

Entry	Samples	Molar ratio (Fe: Cu)	Content of Pd (wt%)
1	Pd/MIL-100(Fe)	–	0.97
2	Pd/MIL-100($Fe_{0.9}Cu_{0.1}$)	0.91:0.09	0.95
3	Pd/MIL-100($Fe_{0.8}Cu_{0.2}$)	0.81:0.19	0.98
4	Pd/MIL-100($Fe_{0.7}Cu_{0.3}$)	0.72:0.28	0.92

2. Experimental section

2.1. Preparation of metal organic frameworks MIL-100(Fe_aCu_b)

In a modified method, MIL-100(Fe_aCu_b) with different mole ratios (a: b) of Fe/Cu were prepared by hydrothermal process. MIL-100 ($Fe_{0.8}Cu_{0.2}$) as a representative sample was prepared by the following process. 1.42 mmol of iron trichloride hexahydrate ($FeCl_3{\cdot}6\ H_2O$), 0.36 mmol of cupric acetate ($Cu_2(CH_3COO)_4$), 1.0 mmol of 1,3,5-benzene tricarboxylate and 10 mL of deionized water were added in a 25 mL Teflon-liner. The mixture solution was vigorously stirred for 25 min and then Teflon-liner was transferred into a steel autoclave which was heated to 150 ℃ for 36 h. The obtained suspension was washed five times with deionized water. The solid was collected by centrifuge and then dried at 60 ℃ for 3 h under a vacuum. MIL-100 ($Fe_{0.9}Cu_{0.1}$) and MIL-100($Fe_{0.7}Cu_{0.3}$) were prepared by the above method.

2.2. Preparation of 1 wt% Pd/MIL-100(Fe_aCu_b)

1 wt% Pd/MIL-100(Fe_aCu_b) was prepared by a photo-deposition process [32]. 100 mg of MIL-100(FeaCub) were dispersed in a bottle with 30 mL of deionized water. Then, 5 mL of methanol was added into the mixture. 168 μL of the solution of H_2PdCl_4 (10 mg mL^{-1}) was added into the above mixture under Ar atmosphere. The bottle was irradiated under a 300 W Xenon lamp for 2 h. The final products were washed with ethanol and deionized water several times. The samples were collected by centrifugation and then dried at 60 ℃ for 12 h. 1 wt% Pd/MIL-100 ($Fe_{0.9}Cu_{0.1}$) and 1 wt% Pd/MIL-100($Fe_{0.7}Cu_{0.3}$) were prepared as contrastive samples by the same method.

2.3. Photocatalytic hydrogenation of cinnamaldehyde

Cinnamaldehyde, acrolein and 3-methyl-2-butenal were used as the representative α, β-unsaturated aldehydes (UAL) for the hydrogenation reaction over the catalysts. As shown in Fig. S1, the photocatalytic process was performed in a H_2 atmosphere (1 atm, 25 ℃) under visible light. 10 mg of the catalyst was dispersed in a reactor with 2 mL of hexane. 0.24 mmol of UAL was added into the reactor. The reactor was full of H_2 and then stirred for 20 min. Finally, the reactor was irradiated by a Xe-arc lamp of 300 W (Microsolar300, 200 mW/cm^2, Beijing Perfectlight Technology Co., Ltd.) with a 420 nm cut-off under stirring for 2 h. Finally, the catalyst removed by a filter membrane. The filtrate was detected by an Agilent gas chromatograph (GC-6890B) with an HP-5 capillary and flame ionization detector (FID).

3. Result and discussion

3.1. Characterization of the prepared samples

Inductively coupled plasma atomic emission spectroscopy (ICP-AES) is used to detected the metals molar ratio of the prepared catalysts. Table 1 displays that the molar ratios of Fe: Cu for the samples are 0.91:0.09, 0.81:0.19 and 0.72:0.28, respectively, suggesting that Cu element is introduced into MIL-100(Fe) successfully. The content of Pd is about 1 wt% in the catalyst. MIL-100(Fe), Pd/MIL-100(Fe), MIL-100 ($Fe_{0.81}Cu_{0.19}$) and Pd/MIL-100($Fe_{0.81}Cu_{0.19}$) are selected as the

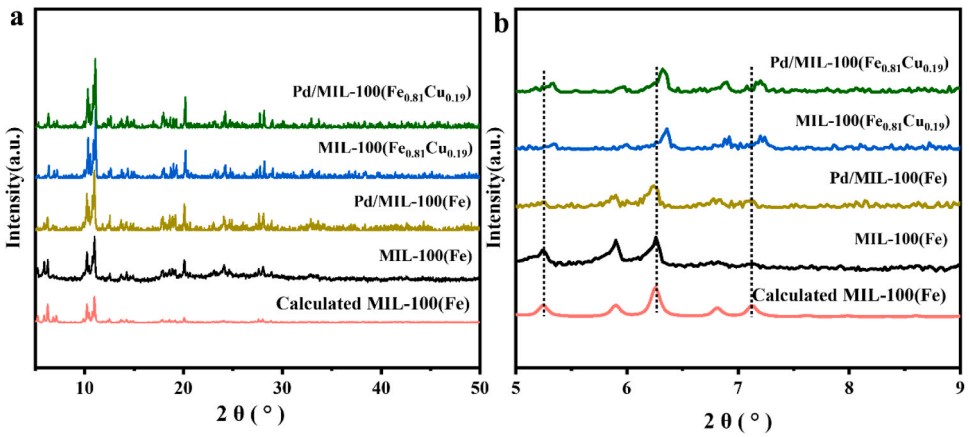

Fig. 1. (a) XRD patterns of the prepared samples; (b) The corresponding expanded XRD plots from 5° to 9°.

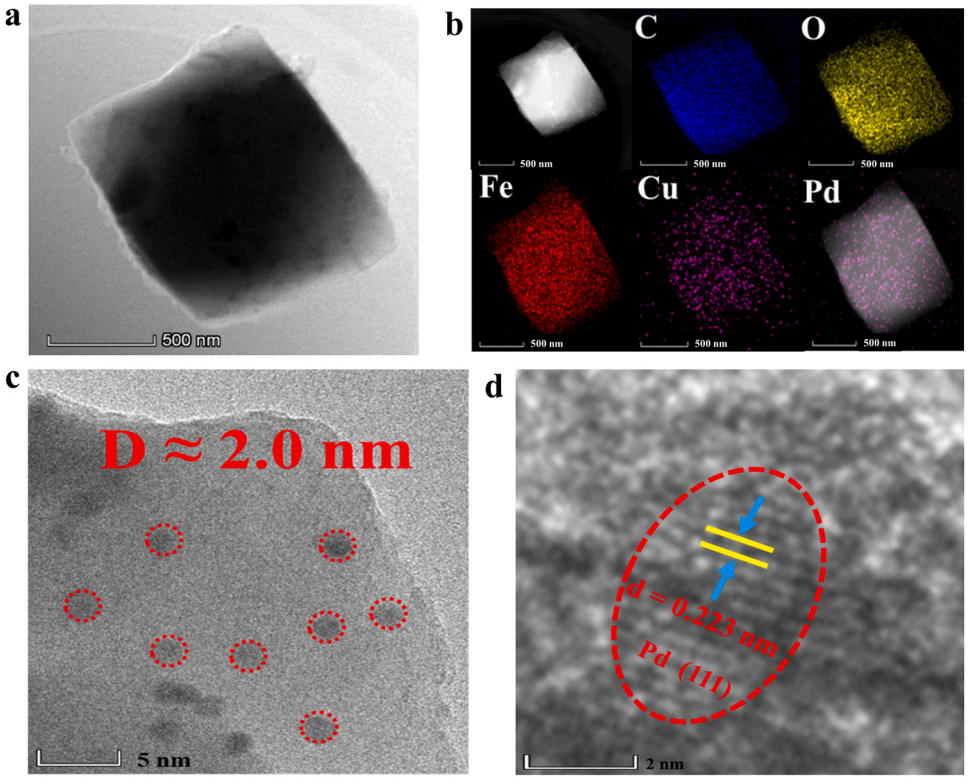

Fig. 2. TEM image (a), energy-dispersive X-ray spectroscopy (EDS) elemental mapping images (b), HR- TEM images (c) and (d) of Pd/MIL-100($Fe_{0.81}Cu_{0.19}$).

representative samples for the characterizations. Other samples are only used as the contrastive catalysts for the evaluation of catalytic performance. The crystalline structure of the catalysts is characterized by powder X-ray diffraction (XRD). Fig. 1a indicates that XRD patterns of the catalysts can be well indexed to the simulated MIL-100(Fe) [33]. Furthermore, there is a little shift to high angle for the diffraction patterns of MIL-100($Fe_{0.81}Cu_{0.19}$) in Fig. 1b, compared with that of MIL-100 (Fe), implying that doping Cu may induce the crystalline structure change of MIL-100(Fe) [34]. Moreover, a significant weakening of the XRD signals can be observed upon doping Cu. It's probably because the doped Cu damage the crystal structure, causing the decrease of crystallinity degree for MIL-100(Fe/Cu). It can be concluded that Cu atoms may be inserted into the lattice of MIL-100(Fe) as the metal nodes, causing the increase of 2θ value. The diffraction patterns of Pd are not observed for Pd/MIL-100($Fe_{0.81}Cu_{0.19}$) and Pd/MIL-100(Fe) because of the little loading mass of 1 wt% [35]. The catalysts with octahedral morphology are obviously observed in the scanning electron microscopy (SEM) (Fig. S2) and transmission electron microscopy (TEM) images (Fig. 2a). In Fig. 2b, the elemental mapping images show that the Fe, Cu, Pd, C and O elements are equably distributed in the Pd/MIL-100 ($Fe_{0.81}Cu_{0.19}$). Moreover, it can be observed that metal clusters with the diameter of about 2 nm are supported on the surface of the catalyst (Fig. 2c). The high-resolution TEM image (Fig. 2d) indicates that the lattice spacing of metal clusters is 0.223 nm, corresponding to the (111) face of Pd [36]. Therefore, 1 wt% Pd/MIL-100(Fe_aCu_b) samples are prepared successfully.

N_2 adsorption/desorption isotherms is carried out for measuring the BET specific surface areas of catalyst. As shown in Fig. S3, MIL-100(Fe) and Pd/MIL-100(Fe) exhibit the large BET specific surface area of 1031 m^2/g and 1028 m^2/g, respectively. MIL-100($Fe_{0.81}Cu_{0.19}$) and Pd/MIL-100($Fe_{0.81}Cu_{0.19}$) are 985 m^2/g and 987 m^2/g, respectively. The IR spectra of the catalysts are displayed in Fig. 3a. The band around

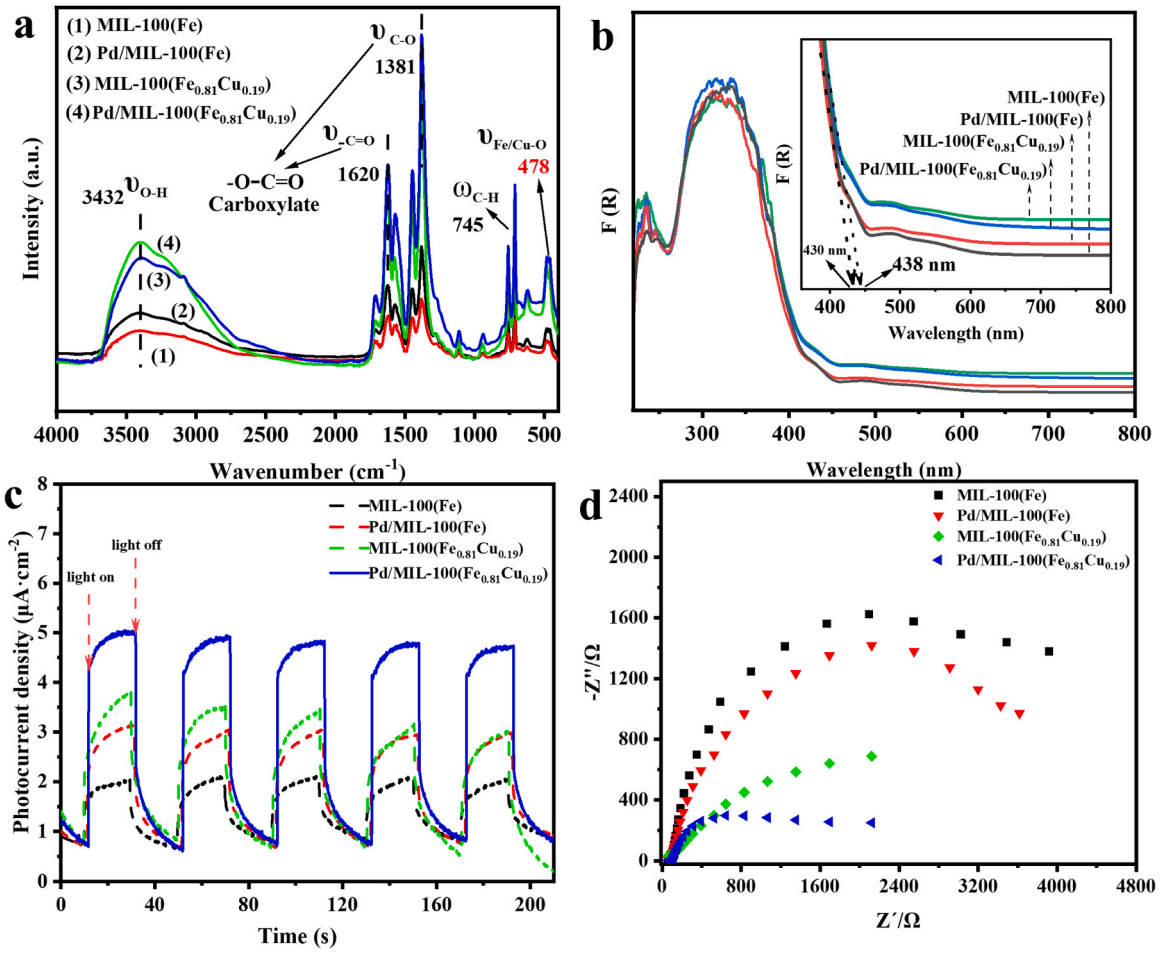

Fig. 3. (a) FT-IR spectra of the samples; (b) UV–vis diffuse reflectance spectra of the samples; (c) Transient photocurrent response of samples under visible light ($\lambda \geq 420$ nm); (d) Nyquist impedance plots of the photocatalysts.

3432 cm^{-1} can be assigned to the stretching vibration of O-H. The peak at 745 cm^{-1} is attributed to the out-of-plane bending vibration of =C-H ($\omega_{=C-H}$) in benzene. The peaks at 1620 and 1381 cm^{-1} belongs to the stretching vibration of C═O and C-O in carboxylate (-CO_2) group. The peak at 478 cm^{-1} may be attributed to the stretching vibration for a metal–oxo bond generated by the Fe (Cu) and carboxylic group [37]. The optical absorption properties of the catalysts are explored by Uv-visible diffuse reflectance spectrum (UV–vis DRS). In Fig. 3b, the samples show a strong absorption of visible light. The absorption region in 300–400 nm can be attributed to the excitation for HOMO to LUMO, while 400–500 nm is the d-d transition for the metal. Compared with the absorption intensity of MIL-100(Fe), the intensity rises at 400–800 nm of MIL-100($Fe_{0.81}Cu_{0.19}$), which may be assigned to the d-d transition of Cu atoms [38,39]. Moreover, the supported Pd clusters cause the increase of absorption intensity at 500–800 nm because of the localized surface plasmon resonance (LSPR) effect of Pd nanoparticles [40]. The photoelectrochemical properties for the catalysts are detected by electrochemical measurement. As shown in Fig. 3c, MIL-100($Fe_{0.81}Cu_{0.19}$) exhibits the higher photo-response current compared with MIL-100(Fe), suggesting that bimetallic nodes (Fe-O-Cu) can facilitates the separation ability of photogenerated electrons-holes. The photo-response current of Pd/MIL-100($Fe_{0.81}Cu_{0.19}$) is higher that of MIL-100($Fe_{0.81}Cu_{0.19}$). The increased photocurrent could be the result of PdNP absorption for the photogeneration electrons [41]. The resistance of the charge transfer for the catalysts is revealed by the electrochemical impedance spectroscopy (EIS). Pd/MIL-100($Fe_{0.81}Cu_{0.19}$) and MIL-100($Fe_{0.81}Cu_{0.19}$) exhibits smaller charge transfer resistance (Fig. 3d) than MIL-100(Fe), suggesting their faster migration velocity for photogenerated carriers. Under light irradiation, Pd nanoparticles can adsorb visible light and hot electrons are generated on Pd surfaces due to the LSPR effect. Moreover, it is well known that the work function of Pd is 5.12 eV higher than that of MIL-100($Fe_{0.81}Cu_{0.19}$). So, a Schottky junction between Pd and MIL-100($Fe_{0.81}Cu_{0.19}$) may be formed in Fig. S4 [40,41]. The photogenerated electrons thus would be transferred to Pd nanoparticles via the Schottky junction as demonstrated by the results of photo-electrochemistry characterizations. Therefore, the photogenerated and hot electrons concentrate on Pd nanoparticles, causing the formation of the electron-rich Pd atoms.

X-ray photoelectron spectroscopy (XPS) is used to investigate the chemical composition and chemical state of each element for the catalysts. In Fig. S5, XPS survey spectra evince the obvious signals of Fe, O and C elements. Moreover, the weak peaks of Pd and Cu elements are observed, resulting from their little content in the samples. The high-resolution Fe 2p spectra (Fig. 3a) show a group of peaks at 724.1 and 710.8 eV, assigned to Fe^{3+} $2p_{1/2}$ and Fe^{3+} $2p_{3/2}$, respectively [33]. O 1s spectra are fitted by adding three peaks at 530.6, 532.0, and 533.8 eV, assigned to the oxygen species of Fe/Cu–O, O-C═O and O-H, respectively (Fig. 3b) [8]. In Cu 2p spectra (Fig. 3c), there are two obvious satellite peaks around 963 and 943 eV. Thus, the peaks (953.1 and 933.5 eV) are corresponded to Cu^{2+} $2p_{1/2}$ and Cu^{2+} $2p_{3/2}$, respectively [42]. Therefore, Cu^{2+} as the metal nodes are introduced into MIL-100 (Fe), which may serve as the active sites for the activation of α, β-unsaturated aldehydes molecule via a Cu···C═C- coordination. The spectra of Pd 3d show two peaks at 335.1 and 346.1 eV (Fig. 3d), attributing to Pd^0 $3d_{3/2}$ and Pd^0 $3d_{5/2}$ [43]. Pd clusters are successfully supported on the catalysts as the active sites for the dissociation of H_2.

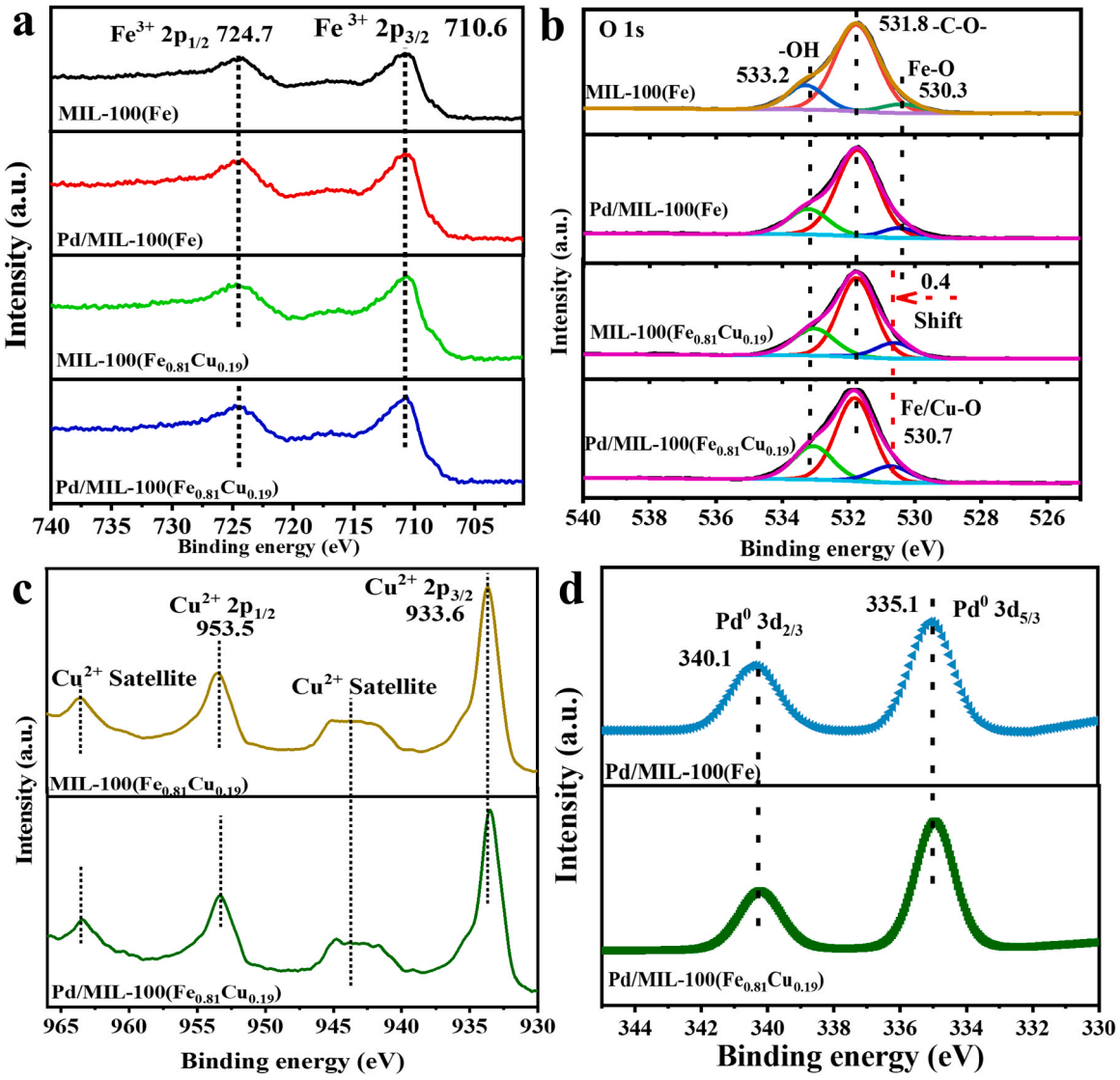

Fig. 4. XPS spectra of the catalysts. (a) Fe 2p; (b) O1s; (c) Cu 2p; (d) Pd 3d;.

3.2. Performances of the prepared catalysts

The photocatalysts performance for hydrogenation of α, β-unsaturated aldehyde (UAL), such as cinnamaldehyde, acrolein and 3-methyl-2-butenal are assessed under visible light in a H_2 atmosphere (1 atm, 25 ℃). As shown in Table 1, the conversion of UAL can be neglected over MIL-100(Fe) because H_2 is not dissociated on the catalyst. Pd/MIL-100(Fe) exhibits a little conversion of UAL (cinnamaldehyde: 3.6 %, acrolein: 5.3 %, 3-methyl-2-butenal: 4.8 %), with a low selectivity of SAL (~20 %). It may be considered that Pd clusters can dissociate H_2 molecules to provide active H for the hydrogenation. After introducing Cu into MIL-100(Fe), MIL-100(Fe_aCu_b) still shows the negligible conversion of UAL because of the absence of Pd. However, when Pd clusters are supported in MIL-100(Fe_aCu_b), Pd/MIL-100($Fe_{0.91}Cu_{0.09}$) show a high selectivity of SAL (>98.0 %) but a low conversion of UAL (~60.0 %). It obviously reveals that Cu can significantly improve the activity and selectivity of the catalyst. The low selectivity may be attributed to the small doping mass of Cu. Then, with the increase of Cu doping, Pd/MIL-100($Fe_{0.81}Cu_{0.19}$) and Pd/MIL-100($Fe_{0.72}Cu_{0.28}$) exhibit the high conversion of UAL (cinnamaldehyde: 99.9 %, acrolein: 99.9 %, 3-methyl-2-butenal: 99.9 %) with a high selectivity of SAL (>97.0 %). These results reveal that Cu^{2+} sites play a critical role to improve the catalytic performance for hydrogeneration UAL to SAL.

Hydrogenation of cinnamaldehyde (CAL) over Pd/MIL-100($Fe_{0.81}Cu_{0.19}$) is served as a representative process to further explore the catalysts performance under different experiment conditions in Table S2. The reaction cannot operate without catalyst or in the dark, proving that the catalytic process is mainly driven by photogenerated carriers. The catalyst cannot effect any conversion of UAL without adding H_2, exhibiting that active [H] species is formed by the dissociation of H_2. Moreover, the Hydrogenation of cinnamaldehyde is carried out in the dark at 25, 40 and 80 ℃ to uncover the thermal effect for the catalysis process. With the rise of temperature, the conversion of cinnamaldehyde gradually increases. At 80 ℃, the conversion is up to 16.4 % whereas 1.9 % at 25 ℃. Our photocatalysis process is executed at 25 ℃, exhibiting the hydrogenation reaction is mainly driven by light irradiation. The selectivity of hydrocinnamaldehyde (HCL) keeps a high level (>98 %) at different temperatures, further confirming that Cu sites of the catalyst determines the chemical selectivity for the hydrogenation of -C═C-. The apparent quantum yield (AQY) for the conversion of UAL is measured using 300 W Xenon lamp with a 420 nm band pass filter [44]. Table S1 shows that The AQY of Pd/MIL-100($Fe_{0.81}Cu_{0.19}$) for UAL reduction is 11.9 %. Moreover, from UV-DRS spectra, the wavelength for plasmonic absorption of PdNPs is high than 500 nm. So, the hydrogeneration reaction of cinnamaldehyde are carried out under light irradiation ($\lambda \geq 500$ nm). In this case, Pd/MIL-100($Fe_{0.81}Cu_{0.19}$)

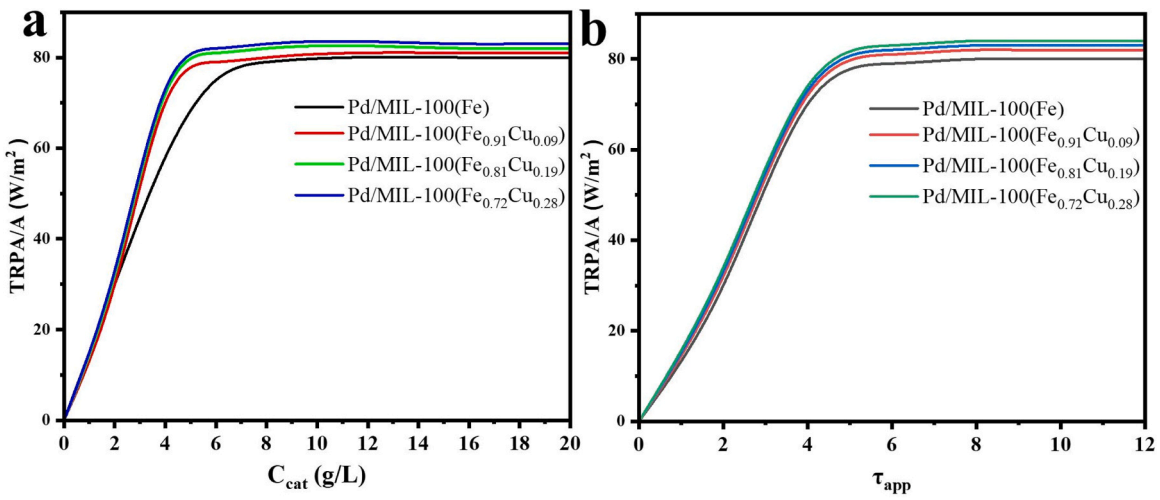

Fig. 5. (a) TRPA per unit of surface area in a planar slurry reactor of thickness L= 1 cm irradiated by light as function of catalyst loading; (b) TRPA per unit of surface area as function of apparent optical thickness for the catalysts.

Table 2
Photocatalytic performance for UAL conversion of prepared samples.

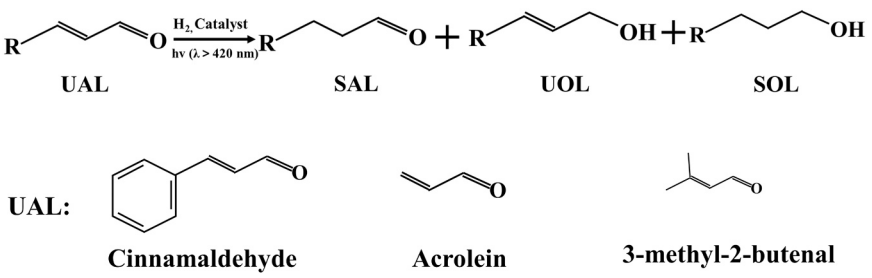

Entry	Photocatalysts	Time (h)	Con. (%)	Sel. (%)		
				SAL	UOL	SOL
Substrate:	UAL					
1	MIL-100(Fe)	2	–	–	–	–
2	MIL-100(Fe_aCu_b)	2	–	–	–	–
Substrate:	cinnamaldehyde					
3	Pd/MIL-100(Fe)	2	3.6	27.1	70.2	0.1
4	Pd/MIL-100($Fe_{0.91}Cu_{0.09}$)	2	58.3	98.3	1.7	–
5	Pd/MIL-100($Fe_{0.81}Cu_{0.19}$)	2	99.9	97.6	1.5	0.9
6	Pd/MIL-100($Fe_{0.72}Cu_{0.28}$)	2	99.9	97.8	1.8	0.4
Substrate:	acrolein					
3	Pd/MIL-100(Fe)	2	5.3	20.1	76.8	3.1
7	Pd/MIL-100($Fe_{0.91}Cu_{0.09}$)	2	62.4	99.2	0.8	–
8	Pd/MIL-100($Fe_{0.81}Cu_{0.19}$)	2	99.9	98.9	0.9	0.2
9	Pd/MIL-100($Fe_{0.72}Cu_{0.28}$)	2	99.9	98.1	1.6	0.3-
Substrate:	3-methyl-2-butenal					
3	Pd/MIL-100(Fe)	2	4.8	19.5	80.2	0.3
10	Pd/MIL-100($Fe_{0.91}Cu_{0.09}$)	2	61.5	99.5	0.5	–
11	Pd/MIL-100($Fe_{0.81}Cu_{0.19}$)	2	99.9	98.6	1.1	0.3
12	Pd/MIL-100($Fe_{0.72}Cu_{0.28}$)	2	99.9	98.7	0.9	0.4

Reaction conditions: UAL (0.24 mmol); catalyst (10 mg); hexamethylene (2 mL); The reactions were conducted under an H2 atmosphere (1 atm) and Xe lamp irradiation (λ > 420 nm) at 25 ℃.

exhibits a conversion of 38.5 % for cinnamaldehyde, with a selectivity of 98.7 % for hydrocinnamaldehyde. The plasmonic absorption of PdNPs is one of the photogenerated electrons sources.

The recyclability and stability of catalysts are explored by a recycling experiment for 5 times over Pd/MIL-100($Fe_{0.81}Cu_{0.19}$) in Fig. S6a. The unattenuated performance reveals the excellent recyclability and stability of the catalyst. Moreover, the used-catalyst are characterized by XRD, TEM and XPS to further explore the catalyst stability. As shown in Fig. S6b, compared with the fresh-catalyst, the XRD pattern of the used catalyst has little change, revealing the crystalline structure of catalyst. TEM images obvious display a MOF crystal with the high dispersed metal clusters (D=2.2 nm) (Fig. S7), indicating that metal clusters are not reunite in the reaction. The XPS spectra of used catalyst show that the chemical states of Fe and Cu for used catalyst are same with that for fresh catalyst (Fig. S8). Therefore, Pd/MIL-100($Fe_{0.81}Cu_{0.19}$) is an excellent catalyst which may have a good potential for industrialization. Fig. 4.

G.L. Puma, et al. reported that the photocatalyst optical properties on the efficiency of solar photocatalytic reactors play the important roles in a photocatalysis system. The six flux model (SFM) is adopted for

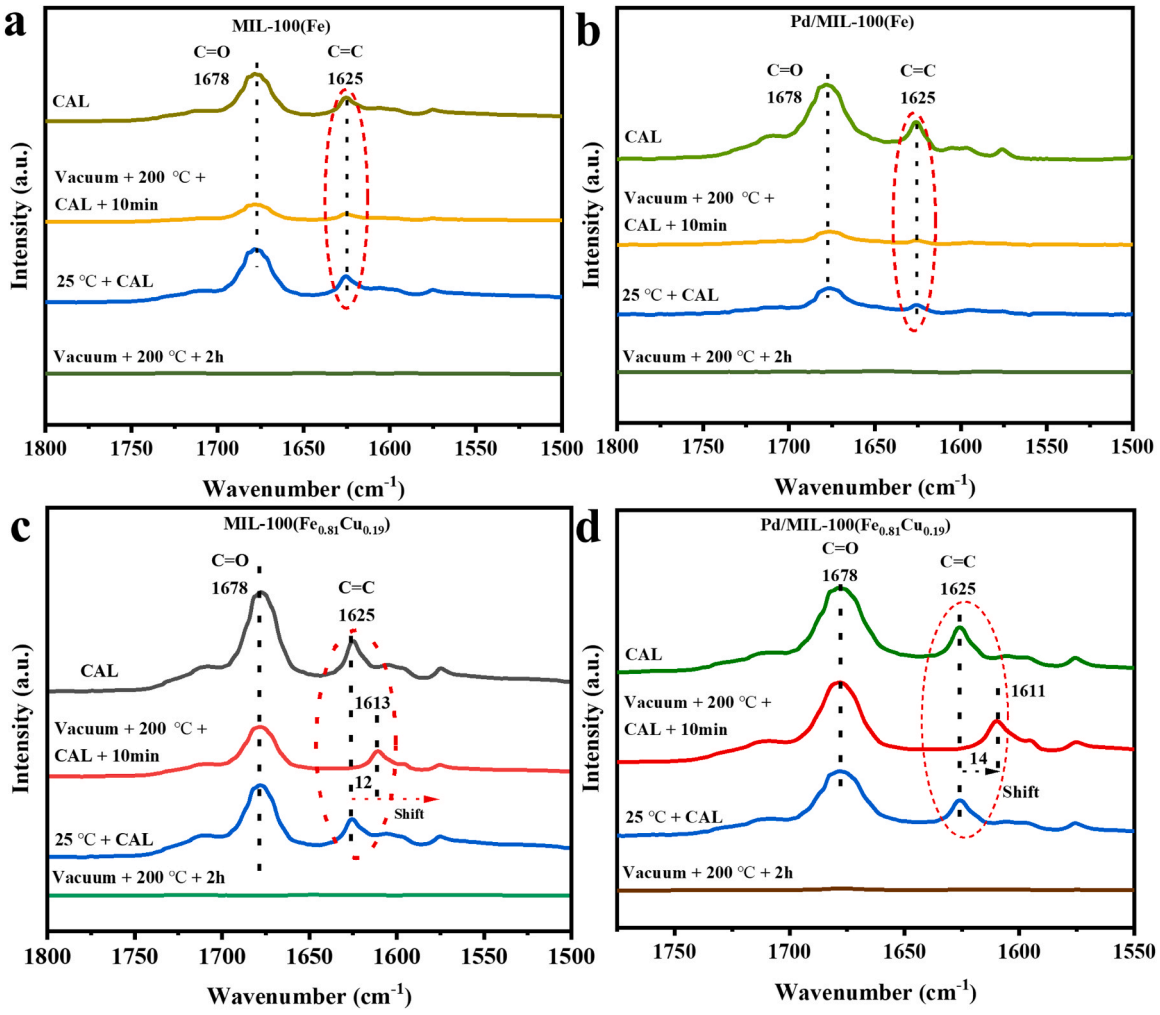

Fig. 6. In situ DRIFTS spectra for the adsorption of CAL on the catalysts: (a) MIL-100(Fe); (b) Pd/MIL-100(Fe); (c)MIL-100($Fe_{0.81}Cu_{0.19}$); (d) Pd/MIL-100 ($Fe_{0.81}Cu_{0.19}$). Conditions: the catalysts were degassed at 200 °C for 2 h. The substrates were adsorbed for 30 min at room temperature (physisorption + chemisorption) and further evacuation of physisorption molecules at 200 °C under 6×10^{-2} kPa (chemisorption).

radiation field calculations [45–48]. The photoreactors characteristics are shown in Table S2. Because MIL-100(Fe) and MIL-100(Fe_aCu_b) cannot exhibit any performance for the reaction, the rate of photon absorption would not be calculated for these samples. The spectral absorption and scattering coefficients of the samples in cyclohexane suspension are shown in Fig. S9, including the light radiation data of Xenon lamp (300 W, $\lambda \geq 420$, 1.6 W/m^2/nm). The optical properties of the photocatalyst are reported in Table S3, together with the corresponding values of the scattering albedo and corrected scattering albedo. The specific scattering (κ^*) and absorption coefficient(σ^*) of the Pd/MIL-100(Fe), Pd/MIL-100($Fe_{0.91}Cu_{0.09}$), Pd/MIL-100($Fe_{0.81}Cu_{0.19}$) and Pd/MIL-100($Fe_{0.72}Cu_{0.28}$) are (28.4, 14.1), (28.5, 13.9), (28.7,

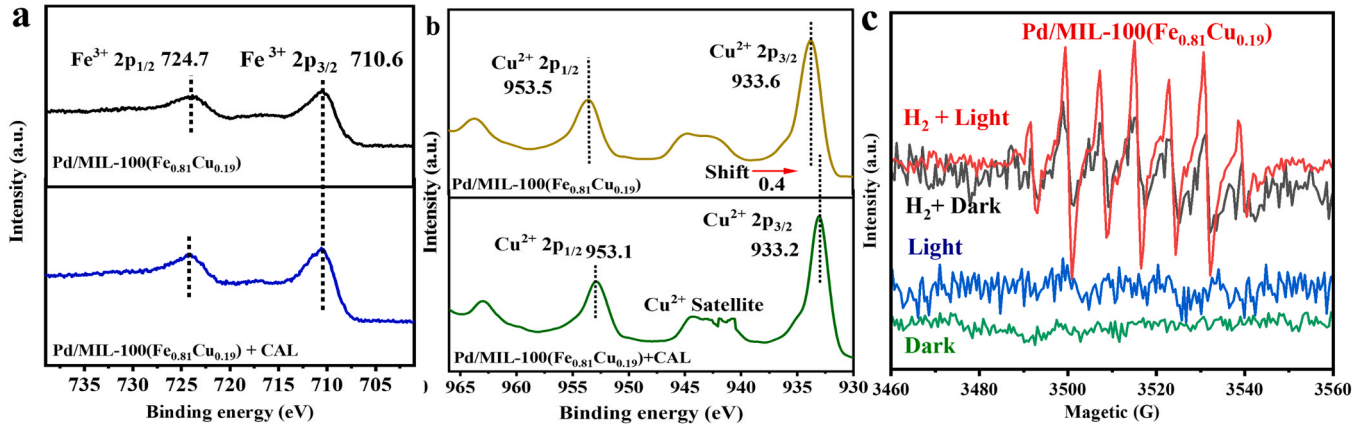

Fig. 7. XPS spectra of MIL-100($Fe_{0.81}Cu_{0.19}$) absorbed cinnamyl alcohol (CAL): (a) Fe 2p; (b) Cu 2p. (c) EPR spectra of Pd/MIL-100($Fe_{0.81}Cu_{0.19}$) in a 2 mL solution (cyclohexane +PBN) with or without light irradiation and adding H_2 ($\lambda > 420$ nm).

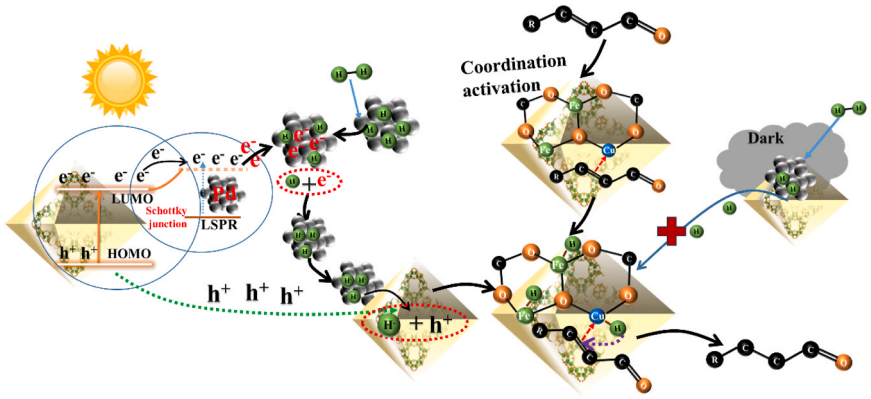

Scheme 2. Photocatalytic mechanism of hydrogenation of α, β-unsaturated aldehydes to saturated aldehyde over Pd/MIL-100($Fe_{0.81}Cu_{0.19}$) under visible light irradiation.

13.5), and (28.8, 13.3), respectively. These similar coefficients indicate that the photocatalysts have the same optical properties. Maximizing the TRPA as a function of the photocatalyst loading can optimize the rate of photon absorption in photoreactors. TRPA/A as a function of the photocatalyst dosage and apparent optical thickness (τ_{app}) is displayed in Fig. 5a and b. The TRPA of all catalysts reached an optimum at a catalyst concentration ($C_{cat} \approx 8.5$ g/L, $\tau_{app} \approx 4.13$). The optimum optical thicknesses of the catalysts are also similar ($\tau_{opt} \approx 5.12$). These results suggest that these parameters used in our experiments are close to the optimal value. So, the obtained results of perform experiments in Table 2 can be considered at equal optical thickness.

3.3. Coordination activation of cinnamaldehyde

To unveil the crucial role of Cu sites for the highly photocatalytic hydrogenation UAL to SAL, cinnamaldehyde (CAL) as the representative reactant molecules are adopted to reveal the coordination activation of α, β-unsaturated aldehyde on the catalyst. In situ Diffused Reflectance Infrared Fourier Transform Spectroscopy (DRIFTS) is used to determine which groups of CAL are coordinated with catalyst. As shown in Fig. 6, the peaks at 1678 and 1625 cm^{-1} belong the stretching vibration of –C═C- and -C═O bonds of free cinnamaldehyde molecules, respectively [49]. For MIL-100(Fe) and Pd/MIL-100(Fe), the absorbed CAL molecules also exhibit two peaks at 1678 and 1625 cm^{-1} (Fig. 6a and b), suggesting –C═C- and -C═O may be not coordinated with catalyst. It can be concluded that Pd and Fe atoms may be not the active sites for the coordination of CAL. However, the bands of -C═C- is at 1613 cm^{-1} and 1611 cm^{-1} in MIL-100($Fe_{0.81}Cu_{0.19}$) and Pd/MIL-100($Fe_{0.81}Cu_{0.19}$), respectively, (Fig. 6c and d). Compared with the vibration peak of -C═C- for free CAL molecules, this peak has a red-shift about 12 cm^{-1}, suggesting that Cu^{2+} nodes induce the coordination of -C═C- with catalyst. To further ascertain the active sites coordinated with -C═C-, the catalysts absorbed CAL molecules are analyzed to detect the charge transfer between the catalyst and cinnamaldehyde by XPS. In Fig. 7a, Fe 2p XPS spectra of Pd/MIL-100($Fe_{0.81}Cu_{0.19}$) absorbed CAL and the pristine Pd/MIL-100($Fe_{0.81}Cu_{0.19}$) exhibit the peaks with the same binding energy, indicating that Fe^{3+} may be not the active sites for absorption of CAL. However, after adoption CAL, the peaks of Cu^{2+} 2p has a shift of 0.4 eV towards to low binding energy (Fig. 7b). It can be concluded that Cu^{2+} obtained additional electrons from the absorbed CAL molecules. Above results reveal that CAL molecules can be selectively activated via a -C═C-···Cu^{2+} coordination. Therefore, our catalysts exhibit a high selectivity for hydrogenation of α, β-unsaturated aldehydes to saturated aldehyde.

3.4. Mechanism of photocatalytic hydrogenation

The generation of H· is explored by Electron paramagnetic resonance (EPR). N-benzylidene-tret-butylamine N-oxide (PBN) is adopted as the spin trap for H·[50]. As shown in Fig. 7c, under dark, the spectra for Pd/MIL-100($Fe_{0.81}Cu_{0.19}$) exhibit a weak group peak which can be assigned to H··PBN species. It reveals that ·H would be produced on the Pd clusters. Under light irradiation, the intensity of these peaks obviously increased, demonstrating that photogenerated carriers can accelerate the formation of active H [51]. The spectra exhibit the negligible signals without adding H_2 under dark or light. Therefore, the active [H] species are not formed by H-atom abstraction from the solvent.

According to above results, a possible mechanism is proposed to interpret the photocatalytic hydrogenation of UAL to SAL. As shown in Scheme 2, there are two pathways for the reaction (light and dark). Under dark, α, β-unsaturated aldehyde molecules are coordinated via selectively binding -C═C- rather than -C═O on Cu^{2+} sites. H_2 are absorbed and dissociated on the Pd atoms to produce H atoms. Pd-bound H atoms cannot migrate directly from Pd to MOF under dark because of the deficiency of driving force and the low concentration of active H. Therefore, the catalysts exhibit negligible activity for the hydrogenation reaction under dark. Under light, the photogenerated carriers generated by the excitation of Fe/Cu-ligands in MOFs and the hot electrons is formed by LSPR of Pd. Because of the Schottky junction between Pd and MOFs, the photogenerated electrons would be transferred to Pd nanoparticles while the holes stay in MOFs. It would cause the formation of electrons-rich PdNPs. The hot and photogenerated electrons would combine with H atoms, causing the production of hydride ion (H^-) [52–55]. The generated H^- may migrate to the MOFs because of their strong activity. The migrated H^- on MOFs would preferentially combine with the holes. H^- thus is oxidized to H atoms on MOFs. Then, H atoms may be attached on the Fe and Cu atoms to generate the Fe-hydride and Cu-hydride species. Therefore, H atoms migrate from Pd to MOF through a photoredox-assisted route. The ligands of MOFs can serve as a bridge for the migration for the active H species and photogenerated carriers. The photogenerated carriers can facilitate the production and migration of active H, thus improving the activity and selectivity for the hydrogenation reaction under light. Because α, β-unsaturated aldehyde molecules are absorbed on Cu atoms of MOFs rather than Fe atoms, H atoms on Cu-hydride would reduce the absorbed α, β-unsaturated aldehyde to saturated aldehyde. Thereby, a whole redox cycle runs in the catalyst.

4. Conclusion

In conclusion, bimetallic nodes Pd/MIL-100(Fe_aCu_b) are successfully constructed for photocatalytic hydrogenation of α, β-unsaturated aldehydes to saturated aldehydes. A typical catalyst, 1 wt% Pd/MIL-100 ($Fe_{0.81}Cu_{0.19}$), exhibits a high conversion of UAL (≈ 100 %), such as cinnamaldehyde, acrolein and 3-methyl-2-butenal, with a high selectivity of SAL (≈ 98 %). The selectivity of target products is determined by a selectively coordination activation between -C═C- and catalyst.

Cinnamaldehyde molecules can be coordinated via binding -C═C- on Cu^{2+} sites. Pd clusters and bimetallic nodes can greatly improve the separation and transfer for photogenerated carriers. The photogenerated carriers accelerate the formation of active H and further enhance the photocatalytic activity. Finally, a possible mechanism for the photocatalytic process has been proposed at a molecular scale. This work provides a valuable pathway for photocatalytic conversion organic to single product assisted by selective coordination activation.

CRediT authorship contribution statement

Zhi-Wen Wang: Conceptualization, Investigation, Formal analysis, Writing - review & editing; **Yue-Yue Kang**: Formal analysis; **Ying-Zhang Shi**: Validation, Formal analysis; **Cheng Liu**: Software, Data curation; **Yunni Liu**: Formal analysis; **Jun Lin:** Conceptualization, Writing - review & editing; **Jinhong Bi:** Writing - review & editing **Ling Wu:** Conceptualization, Writing - review & editing.

Declaration of Competing Interest

The authors declare no competing financial interest.

Data Availability

No data was used for the research described in the article.

Acknowledgements

This work was supported by the National Natural Science Foundation of China (22272026, 22272028). Jinhong Bi thanks the Youth Talent Support Program of Fujian Province, China (00387077).

Appendix A. Supporting information

Supplementary data associated with this article can be found in the online version at doi:10.1016/j.apcatb.2023.123162.

References

[1] M. Luneau, J.S. Lim, D.A. Patel, E.C.H. Sykes, C.M. Friend, P. Sautet, Guidelines to achieving high selectivity for the hydrogenation of α, β-unsaturated aldehydes with bimetallic and dilute alloy catalysts: a review, Chem. Rev. 120 (2020) 12834–12872, https://doi.org/10.1021/acs.chemrev.0c00582.

[2] X. Lan, T. Wang, Highly selective catalysts for the hydrogenation of unsaturated aldehydes: a review, ACS Catal. 10 (2020) 2764–2790, https://doi.org/10.1021/acscatal.9b04331.

[3] F. Wang, Y. Bi, K. Hu, X. Wei, Pd nanoparticles supported on triangle-shaped $La_2O_2CO_3$ nanosheets: a new highly efficient and durable catalyst for selective hydrogenation of cinnamaldehyde to hydrocinnamaldehyde, Chem. Eur. J. 26 (2020) 4874–4879, https://doi.org/10.1002/chem.202000741.

[4] S. Bewana, M.J. Ndolomingo, E. Carleschi, B.P. Doyle, R. Meijboom, N. Bingwa, Inorganic perovskite-induced synergy on highly selective Pd-catalyzed hydrogenation of cinnamaldehyde, ACS Appl. Mater. Interfaces 11 (2019) 32994–33005, https://doi.org/10.1021/acsami.9b10820.

[5] T. Jia, D. Meng, R. Duan, H. Ji, H. Sheng, C. Chen, J. Li, W. Song, J. Zhao, Single-atom nickel on carbon nitride photocatalyst achieves semihydrogenation of alkynes with water protons via monovalent nickel, Angew. Chem. Int. Ed. 100049 (2023) 1–10, https://doi.org/10.1002/anie.202216511.

[6] E. Zhao, M. Li, B. Xu, X.L. Wang, Y. Jing, D. Ma, S. Mitchell, J. Pérez-Ramírez, Z. Chen, Transfer hydrogenation with a carbon-nitride-supported palladium single-atom photocatalyst and water as a proton source, Angew. Chem. Int. Ed. 61 (2022), https://doi.org/10.1002/anie.202207410.

[7] C.H. Hao, X.N. Guo, Y.T. Pan, S. Chen, Z.F. Jiao, H. Yang, X.Y. Guo, Visible-light-driven selective photocatalytic hydrogenation of cinnamaldehyde over Au/SiC catalysts, J. Am. Chem. Soc. 138 (2016) 9361–9364, https://doi.org/10.1021/jacs.6b04175.

[8] Y. Kang, Z. Wang, Y. Shi, B. Guo, L. Wu, Synthesis of aluminum doped MIL-100(Fe) compounds for the one-pot photocatalytic conversion of cinnamaldehyde and benzyl alcohol to the corresponding alcohol and aldehyde under anaerobic conditions, J. Catal. 406 (2022) 184–192, https://doi.org/10.1016/j.jcat.2022.01.010.

Y. Lv, M. Han, W. Gong, D. Wang, C. Chen, G. Wang, H. Zhang, H. Zhao, Fe-Co alloyed nanoparticles catalyzing efficient hydrogenation of cinnamaldehyde to cinnamyl alcohol in water, Angew. Chem. Int. Ed. 59 (2020) 23521–23526, https://doi.org/10.1002/anie.202009913.

[10] Z. Li, W. Wei, H. Li, S. Li, L. Leng, M. Zhang, J.H. Horton, D. Wang, W. Sun, C. Guo, W. Wu, J. Wang, Low-temperature synthesis of single palladium atoms supported on defective hexagonal boron nitride nanosheet for chemoselective hydrogenation of cinnamaldehyde, ACS Nano 15 (2021) 10175–10184, https://doi.org/10.1021/acsnano.1c02094.

[11] H. Wang, Y. Shi, Z. Wang, Y. Song, M. Shen, B. Guo, L. Wu, Selective hydrogenation of cinnamaldehyde to hydrocinnamaldehyde over Au-Pd/ultrathin $SnNb_2O_6$ nanosheets under visible light, J. Catal. 396 (2021) 374–386.

[12] Y. Dai, X. Gao, X. Chu, C. Jiang, Y. Yao, Z. Guo, C. Zhou, C. Wang, H. Wang, Y. Yang, On the role of water in selective hydrogenation of cinnamaldehyde to cinnamyl alcohol on PtFe catalysts, J. Catal. 364 (2018) 192–203, https://doi.org/10.1016/j.jcat.2018.05.008.

[13] H. Wang, B. Liu, F. Liu, Y. Wang, X. Lan, S. Wang, B. Ali, T. Wang, Transfer hydrogenation of cinnamaldehyde catalyzed by Al_2O_3 using ethanol as a solvent and hydrogen donor, ACS Sustain. Chem. Eng. 8 (2020) 8195–8205, https://doi.org/10.1021/acssuschemeng.0c00942.

[14] X. Wang, X. Liang, P. Geng, Q. Li, Recent advances in selective hydrogenation of cinnamaldehyde over supported metal-based catalysts, ACS Catal. 10 (2020) 2395–2412, https://doi.org/10.1021/acscatal.9b05031.

[15] L. Zhang, M. Zhou, A. Wang, T. Zhang, Selective hydrogenation over supported metal catalysts: from nanoparticles to single atoms, Chem. Rev. 120 (2020) 683–733, https://doi.org/10.1021/acs.chemrev.9b00230.

[16] Y. Shi, Z. Wang, C. Liu, T. kang Wu, R. Liu, L. Wu, Surface synergetic effects of Pt clusters/monolayer Bi_2MoO_6 nanosheet for promoting the photocatalytic selective reduction of 4-nitrostyrene to 4-vinylaniline, Appl. Catal. B Environ. 304 (2021), 121010, https://doi.org/10.1016/j.apcatb.2021.121010.

[17] S. Liang, L. Wen, S. Lin, J. Bi, P. Feng, X. Fu, L. Wu, Monolayer HNb_3O_8 for selective photocatalytic oxidation of benzylic alcohols with visible light response, Angew. Chem. Int. Ed. 53 (2014) 2951–2955, https://doi.org/10.1002/anie.201311280.

[18] Y. Song, H. Wang, Z. Wang, B. Guo, K. Jing, Y. Li, L. Wu, Selective photocatalytic synthesis of haloanilines from halonitrobenzenes over multifunctional AuPt/monolayer titanate nanosheet, ACS Catal. 8 (2018) 9656–9664, https://doi.org/10.1021/acscatal.8b02662.

[19] Z.W. Wang, Q. Wan, Y.Z. Shi, H. Wang, Y.Y. Kang, S.Y. Zhu, S. Lin, L. Wu, Selective photocatalytic reduction CO_2 to CH_4 on ultrathin TiO_2 nanosheet via coordination activation, Appl. Catal. B Environ. 288 (2021), 120000, https://doi.org/10.1016/j.apcatb.2021.120000.

[20] Y. Lv, M. Han, W. Gong, D. Wang, C. Chen, G. Wang, H. Zhang, H. Zhao, Fe-Co alloyed nanoparticles catalysed efficient hydrogenation of cinnamaldehyde to cinnamyl alcohol in water, Angew. Chem. Int. Ed. 59 (2020) 23521–23526, https://doi.org/10.1002/anie.202009913.

[21] Q. Wang, D. Astruc, State of the art and prospects in metal-organic framework (MOF)-based and MOF-derived nanocatalysis, Chem. Rev. 120 (2020) 1438–1511, https://doi.org/10.1021/acs.chemrev.9b00223.

[22] Z. Zhang, J. Jia, Y. Zhi, S. Ma, X. Liu, Porous organic polymers for light-driven organic transformations, Chem. Soc. Rev. 51 (2022) 2444–2490, https://doi.org/10.1039/d1cs00808k.

[23] M. Ding, R.W. Flaig, H.L. Jiang, O.M. Yaghi, Carbon capture and conversion using metal-organic frameworks and MOF-based materials, Chem. Soc. Rev. 48 (2019) 2783–2828, https://doi.org/10.1039/c8cs00829a.

[24] J.H. Fu, Z. Zhong, D. Xie, Y.J. Guo, D.X. Kong, Z.X. Zhao, Z.X. Zhao, M. Li, SERS-active MIL-100(Fe) sensory array for ultrasensitive and multiplex detection of VOCs, Angew. Chem. Int. Ed. 59 (2020) 20489–20498, https://doi.org/10.1002/anie.202002720.

[25] T. Wu, Y. Shi, Z. Wang, C. Liu, J. Bi, Y. Yu, L. Wu, Unsaturated Ni^{II} centers mediated the coordination activation of benzylamine for enhancing photocatalytic activity over ultrathin Ni MOF-74 nanosheets, ACS Appl. Mater. Interfaces 13 (2021) 61286–61295, https://doi.org/10.1021/acsami.1c20128.

[26] B. Guo, X. Cheng, Y. Tang, W. Guo, S. Deng, L. Wu, X. Fu, Metal–Organic Frameworks Hot Paper Dehydrated UiO-66 (SH)2: The Zr-O Cluster and Its Photocatalytic, 350002 (2022).

[27] J. Li, H. Huang, W. Xue, K. Sun, X. Song, C. Wu, L. Nie, Y. Li, C. Liu, Y. Pan, H. L. Jiang, D. Mei, C. Zhong, Self-adaptive dual-metal-site pairs in metal-organic frameworks for selective CO_2 photoreduction to CH_4, Nat. Catal. 4 (2021) 719–729, https://doi.org/10.1038/s41929-021-00665-3.

[28] S. Dissegna, K. Epp, W.R. Heinz, G. Kieslich, R.A. Fischer, Defective metal-organic frameworks, Adv. Mater. 30 (2018) 1–23, https://doi.org/10.1002/adma.201704501.

[29] G. Zhong, D. Liu, J. Zhang, Applications of porous metal-organic framework MIL-100(M) (M = Cr, Fe, Sc, Al, V), Cryst. Growth Des. 18 (2018) 7730–7744, https://doi.org/10.1021/acs.cgd.8b01353.

[30] Q. Wu, H. Ma, Y. Wang, J. Chen, J. Dai, X. Xu, X. Wu, Surface electron localization in Cu-MOF-bonded double-heterojunction Cu_2O induces highly efficient photocatalytic CO_2 reduction, ACS Appl. Mater. Interfaces 14 (2022) 54328–54337, https://doi.org/10.1021/acsami.2c15278.

[31] Z.F. Jiao, X.N. Guo, Z.Y. Zhai, G.Q. Jin, X.M. Wang, X.Y. Guo, The enhanced catalytic performance of Pd/SiC for the hydrogenation of furan derivatives at ambient temperature under visible light irradiation, Catal. Sci. Technol. 4 (2014) 2494–2498, https://doi.org/10.1039/c4cy00275j.

[32] Y. Shi, H. Wang, Z. Wang, T. Wu, Y. Song, B. Guo, L. Wu, Pt decorated hierarchical Sb_2WO_6 microspheres as a surface functionalized photocatalyst for the visible-light-driven reduction of nitrobenzene to aniline, J. Mater. Chem. A 8 (2020) 18755–18766, https://doi.org/10.1039/d0ta06099b.

[33] P. Horcajada, S. Surblé, C. Serre, D.Y. Hong, Y.K. Seo, J.S. Chang, J.M. Grenèche, I. Margiolaki, G. Férey, Synthesis and catalytic properties of MIL-100(Fe), an iron (III) carboxylate with large pores, Chem. Commun. 100 (2007) 2820–2822, https://doi.org/10.1039/b704325b.
[34] Y. Shi, M. Shen, Z. Wang, C. Liu, J. Bi, L. Wu, Visible-light-driven benzyl alcohol oxidation over Pt/Mn-$Bi_4Ti_3O_{12}$ nanosheets: structure-function relationship of multicomponent photocatalysts, J. Catal. 418 (2023) 141–150, https://doi.org/10.1016/j.jcat.2023.01.015.
[35] W. Guo, Y. Qin, C. Liu, B. Guo, J. Zou, Z. Xie, L. Wu, Unveiling the intermediates/pathways towards photocatalytic dechlorination of 3,3′,4,4′-trtrachlorobiphenyl over Pd /TiO_2(B) nanosheets, Appl. Catal. B Environ. 298 (2021), 120526, https://doi.org/10.1016/j.apcatb.2021.120526.
[36] S. Fujiwara, N. Takanashi, R. Nishiyabu, Y. Kubo, Boronate microparticle-supported nano-palladium and nano-gold catalysts for chemoselective hydrogenation of cinnamaldehyde in environmentally preferable solvents, Green. Chem. 16 (2014) 3230–3236, https://doi.org/10.1039/c4gc00383g.
[37] W. Liu, J. Zhou, D. Liu, S. Liu, X. Liu, S. Xiao, C. Feng, C. Leng, Fe-MOF by ligand selective pyrolysis for Fenton-like process and photocatalysis: accelerating effect of oxygen vacancy, J. Taiwan Inst. Chem. Eng. 127 (2021) 327–333, https://doi.org/10.1016/j.jtice.2021.08.002.
[38] Y. Wang, H. Lv, E.S. Grape, C.A. Gaggioli, A. Tayal, A. Dharanipragada, T. Willhammar, A.K. Inge, X. Zou, B. Liu, Z. Huang, A. Tunable, Multivariate metal-organic framework as a platform for designing photocatalysts, J. Am. Chem. Soc. 143 (2021) 6333–6338, https://doi.org/10.1021/jacs.1c01764.
[39] Z. Wang, J.J. Liu, S.Y. Yin, M.Y. Li, Y.J. Hou, D. Wang, J.T. Mo, G. Chen, Ultralong near infrared room temperature phosphorescence in Cu(I) metal-organic framework based-on D–π–A–π–D linkers, Adv. Funct. Mater. 2212985 (2023) 1–8, https://doi.org/10.1002/adfm.202212985.
[40] D. Wu, K. Deng, B. Hu, Q. Lu, G. Liu, X. Hong, Plasmon-assisted photothermal catalysis of low-pressure CO_2 hydrogenation to methanol over Pd/ZnO catalyst, ChemCatChem 11 (2019) 1598–1601, https://doi.org/10.1002/cctc.201802081.
[41] Y. Song, H. Wang, X. Gao, Y. Feng, S. Liang, J. Bi, S. Lin, X. Fu, L. Wu, A Pd/monolayer titanate nanosheet with surface synergetic effects for precise synthesis of cyclohexanones, ACS Catal. 7 (2017) 8664–8674, https://doi.org/10.1021/acscatal.7b03463.
[42] D. Han, Y. Han, J. Li, X. Liu, K.W.K. Yeung, Y. Zheng, Z. Cui, X. Yang, Y. Liang, Z. Li, S. Zhu, X. Yuan, X. Feng, C. Yang, S. Wu, Enhanced photocatalytic activity and photothermal effects of cu-doped metal-organic frameworks for rapid treatment of bacteria-infected wounds, Appl. Catal. B Environ. 261 (2020), 118248, https://doi.org/10.1016/j.apcatb.2019.118248.
[43] K. Chen, Z. Ma, X. Li, J. Kang, D. Ma, K. Chu, Single-atom Bi alloyed Pd metallene for nitrate electroreduction to ammonia, Adv. Funct. Mater. 2209890 (2023) 1–8, https://doi.org/10.1002/adfm.202209890.
[44] Z.A. Lan, M. Wu, Z. Fang, X. Chi, X. Chen, Y. Zhang, X. Wang, A fully coplanar donor–acceptor polymeric semiconductor with promoted charge separation kinetics for photochemistry, Angew. Chem. Int. Ed. 60 (2021) 16355–16359, https://doi.org/10.1002/anie.202103992.
[45] J. Colina-Márquez, F. Machuca-Martínez, G. Li Puma, Photocatalytic mineralization of commercial herbicides in a pilot-scale solar CPC reactor: photoreactor modeling and reaction kinetics constants independent of radiation field, Environ. Sci. Technol. 43 (2009) 8953–8960, https://doi.org/10.1021/es902004b.
[46] I. Grčić, G.Li Puma, Six-flux absorption-scattering models for photocatalysis under wide-spectrum irradiation sources in annular and flat reactors using catalysts with different optical properties, Appl. Catal. B Environ. 211 (2017) 222–234, https://doi.org/10.1016/j.apcatb.2017.04.014.
[47] R. Acosta-Herazo, M.Á. Mueses, G.L. Puma, F. Machuca-Martínez, Impact of photocatalyst optical properties on the efficiency of solar photocatalytic reactors rationalized by the concepts of initial rate of photon absorption (IRPA) dimensionless boundary layer of photon absorption and apparent optical thickness, Chem. Eng. J. 356 (2019) 839–849, https://doi.org/10.1016/j.cej.2018.09.085.
[48] L. Hurtado, R. Natividad, E. Torres-García, J. Farias, G. Li Puma, Correlating the photocatalytic activity and the optical properties of $LiVMoO_6$ photocatalyst under the UV and the visible region of the solar radiation spectrum, Chem. Eng. J. 262 (2015) 1284–1291, https://doi.org/10.1016/j.cej.2014.10.052.
[49] H. Liu, Z. Li, Y. Li, Chemoselective hydrogenation of cinnamaldehyde over a Pt-Lewis acid collaborative catalyst under ambient conditions, Ind. Eng. Chem. Res. 54 (2015) 1487–1497, https://doi.org/10.1021/ie504357r.
[50] A.F. Carley, H.A. Edwards, B. Mile, M.W. Roberts, C.C. Rowlands, S.D. Jackson, F. E. Hancock, An EPR study of a palladium catalyst using a PBN (N-benzylidene-tert-butylamine N-oxide) spin trap: direct demonstration of hydrogen spillover, J. Chem. Soc. Chem. Commun. (1994) 1407–1408, https://doi.org/10.1039/C39940001407.
[51] Y. Shi, T. Wu, Z. Wang, C. Liu, J. Bi, L. Wu, Photocatalytic precise hydrogenation of furfural over ultrathin Pt/NiMg-MOF-74 nanosheets: synergistic effect of surface optimized Ni^{II} sites and Pt clusters, Appl. Surf. Sci. 616 (2023), 156553, https://doi.org/10.1016/j.apsusc.2023.156553.
[52] S. Matsuishi, K. Hayashi, M. Hirano, H. Hosono, Hydride ion as photoelectron donor in microporous crystal, J. Am. Chem. Soc. 127 (2005) 12454–12455, https://doi.org/10.1021/ja053568m.
[53] Q. Wu, C. Zhang, M. Arai, B. Zhang, R. Shi, P. Wu, Z. Wang, Q. Liu, K. Liu, W. Lin, H. Cheng, F. Zhao, Pt/TiH_2 catalyst for ionic hydrogenation via stored hydrides in the presence of gaseous H_2, ACS Catal. 9 (2019) 6425–6434, https://doi.org/10.1021/acscatal.9b00917.
[54] L. Zhang, M. Zhou, A. Wang, T. Zhang, Selective hydrogenation over supported metal catalysts: from nanoparticles to single atoms, Chem. Rev. 120 (2020) 683–733, https://doi.org/10.1021/acs.chemrev.9b00230.
[55] P. Liu, Y. Zhao, R. Qin, S. Mo, G. Chen, L. Gu, D.M. Chevrier, P. Zhang, Q. Guo, D. Zang, B. Wu, G. Fu, N. Zheng, Catalysis: photochemical route for synthesizing atomically dispersed palladium catalysts, Science 352 (2016) 797–801, https://doi.org/10.1126/science.aaf5251.